Investigation into the aerodynamic performance of a concept sports car

Mike Dickison[1], Mohammad Ghaleeh[2], Soliman Milady[1], Shreeharsha Subbakrishna[1], Lit Tan Wen[1] and Mansour Al Qubeissi[1†]

[1]*Faculty of Engineering, Environment and Computing, Coventry University, Coventry, United Kingdom*
[2]*Department of Engineering, University of Northampton, Northampton, United Kingdom*

ABSTRACT

Transport aerodynamic optimisation has become an increasingly important field of study in response to emerging factors, such as new human needs and market demands. This paper provides a concept in-house built sports-car aerodynamic and shape optimisation. Wind tunnel tests and numerical simulations have been set-up and conducted to understand the concept vehicle aerodynamic structure and needs for performance improvement. A computer-aided design model has been developed and implemented into the computational fluid dynamics (CFD) software of StarCCM+ for detailed analysis. A 1/4th full-scale fibreglass model has been manufactured for validation. The combined experimental and CFD analyses show that the original aesthetic design exhibits high rear-end lift-force. Modifications have been assessed to improve the drag and lift forces for the front, middle and rear regions. Several geometrical changes are introduced, including new rear-wing design. Also, the front end, roof profile and various ducting modifications have been considered. The introduced design changes lead to optimised downforce of -560.18 N with negligible increase to the accumulated drag effects with $C_D \leq 0.3$.

GRAPHICAL ABSTRACT
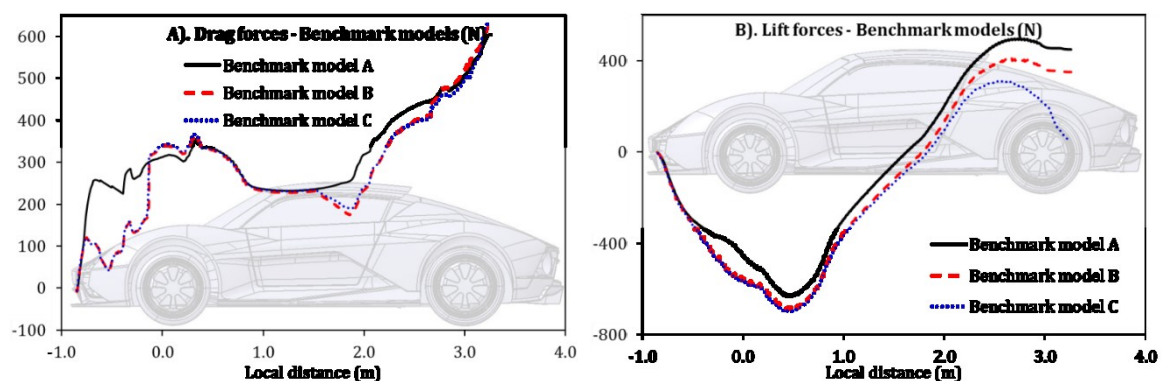
Keywords: Aerodynamics; CFD modelling; Drag-force; Downforce; Light-weighting.

† *Corresponding Author Email: ac1028@coventry.ac.uk; Tel. +44-2477-65-8060.*

1. Introduction

The understanding of vehicle aerodynamics is essential for ensuring good driving performance and safety (Kodiyalam & Sobieszczanski-Sobieski, 2001; Buljac *et al.*, 2016; Han *et al.*, 2014; Yang *et al.*, 2018). There have been many studies on ground vehicle aerodynamics and optimisation during the last decade (Ahmed *et al.*, 1985; Mohrfeld-Halterman & Uddin, 2016a; Marchesin *et al.*, 2017), but with the continuous developments, research in this topic remains of great importance to the public and industry (Katz, 2006; Khaled *et al.*, 2012; Hassan *et al.*, 2014). Those contributions have been stimulated by the utilization of high computer aided simulation capacities. Such advancement is yielding several important improvements in design and thermo-fluid efficiencies (Skinner & Zare-Behtash, 2018; Zhang *et al.*, 2018). In a sports car design process, the aerodynamics of such light weight vehicles must be seriously considered to minimize drag forces and maximize high-speed down forces for safety (Tsai *et al.*, 2009; Huminic *et al.*, 2012; Sadeghizadeh *et al.*, 2017).

Aerodynamics of sports cars is mainly characterised by their shape and airflow over surfaces and body ducts (Hucho & Aerodynamik, 1987; Road Vehicle Aerodynamics Forum Committee, 1994). Benchmark of existing sports cars illustrates a common feature, whereby air is directed to flow from the front to the end of the car smoothly, creating a minimum drag-inducing wake. The key aerodynamic parameters used in designing sports cars are that (Goetz, 1971; Hucho & Aerodynamik, 1987; Buljac *et al.*, 2016; Mohrfeld-Halterman & Uddin, 2016a): the frontal area of the vehicle is in direct proportion to the overall drag force; determining a balance between minimising overall drag or increasing negative lift (downforce), normally high speed sports cars would require a higher negative lift-to-drag ratio; rear downforce to front downforce ratio optimisation (CLR: CLF) is needed to ensure the stability and maneuverability of the car. However, the front lift coefficient CLF should be kept below or close to zero to prevent understeering; an overall

vehicle down force is important, to ensure that the tyres remain in firm contact with the ground, thus enhancing grip; and an effective cooling and ventilating system is achieved without significantly adversely affecting the aerodynamic performance.

The latter factors are taken into account in our analysis. The governing equations used for the CFD model are mainly based on the RANS model (the basic equations are presented in Appendix A). The work methodology of experimental and modelling set ups is presented in Section 2. The results, including CFD validation, are presented in Section 3. The results are summarised and final conclusions are made in Section 4. Further illustrative figures about optimisation, meshing and design aspects are presented in Appendices B, C and D, respectively.

2. Methodology

In our analysis, the full scale (Sparrowhawk) sports-car is accounted for, instead of the prototype vehicle used in the wind tunnel experiment. Therefore, the facilitated wind tunnel for experiment is modelled in a full (virtual) scale aerodynamic CFD simulation. Mesh type and accuracy has been carefully considered with optimisation. In what follows, the descriptions of wind tunnel, car design and meshing are provided.

2.1 Wind Tunnel Set-Up

Wind tunnel testing was conducted in an open test section closed return wind tunnel with a working throat area of 1.1 m × 1.3 m (see Table 1 for dimensions). Testing was conducted on a twenty five percent full scale models of a lightweight sports car, manufactured in fiberglass. The model was attached to an overhead balance through a strut with an aerofoil shape to minimize wind resistance. The model was tested at various wind speeds (25 – 45 m/s). The results obtained as raw data from the Diablo software were used to calculate the drag and lift coefficients (C_D, C_L) and forces, pitch moment coefficients and the downforce distribution.

Table 1. Dimension of the tested car model.

Description	Dimension

Model width	455 mm
Model height	290 mm
Model length	1025 mm
Frontal area	0.108 m^2
Distance – Al plate & bottom-tip of wheels	5 mm
Length of Aluminium plate	1209 mm
Width of Aluminium plate	750 mm
Thickness of Aluminium plate	6 mm

2.2 Shape design

CAD models of the lightweight sports car were created. A commercial CFD software of Star-CCM+ was used for the 3D simulation work. The CFD software facilitates the fundamental fluid mechanics principles, the governing equations of which are presented in Appendix A. In order to achieve a more realistic simulation, internal components of the car (radiator, engine, intercooler stock and chassis) were incorporated into the analysis. The components were simplified and constructed in CAD. The final design is shown in Figure 1 (See Appendix B (e.g., Figure B.2), for the CFD implemented wind tunnel size for the full car model). The dimensions of the virtual wind tunnel were set to be 2L × 8L × 2L (L is the length of the car model), inferred from recent research data (Rao *et al.*, 2007; Huminic & Huminic, 2008; Christoffersen *et al.*, 2010; Buscariolo & Karbon, 2011; Koitrand *et al.*, 2014; Das & Riyad, 2017) as: 2L from the front of the car, 5L behind the car, 2L as the width of the wind tunnel, L from the centre of car (in full size) and 2L for the height from the ground of virtual wind tunnel. Dimension above considered the blockage ratio $\left(\frac{\text{Frontal area of the model}}{\text{Cross section area of virtual wind tunnel}} \times 100 \right)$ smaller than 5% (Road Vehicle Aerodynamics Forum Committee, 1994). The simulations were carried out with the car model. The hydraulic diameter, reported in (Mohrfeld-Halterman & Uddin, 2016b; Pirozzoli, 2018), is taken into account for the tunnel and model design considerations.
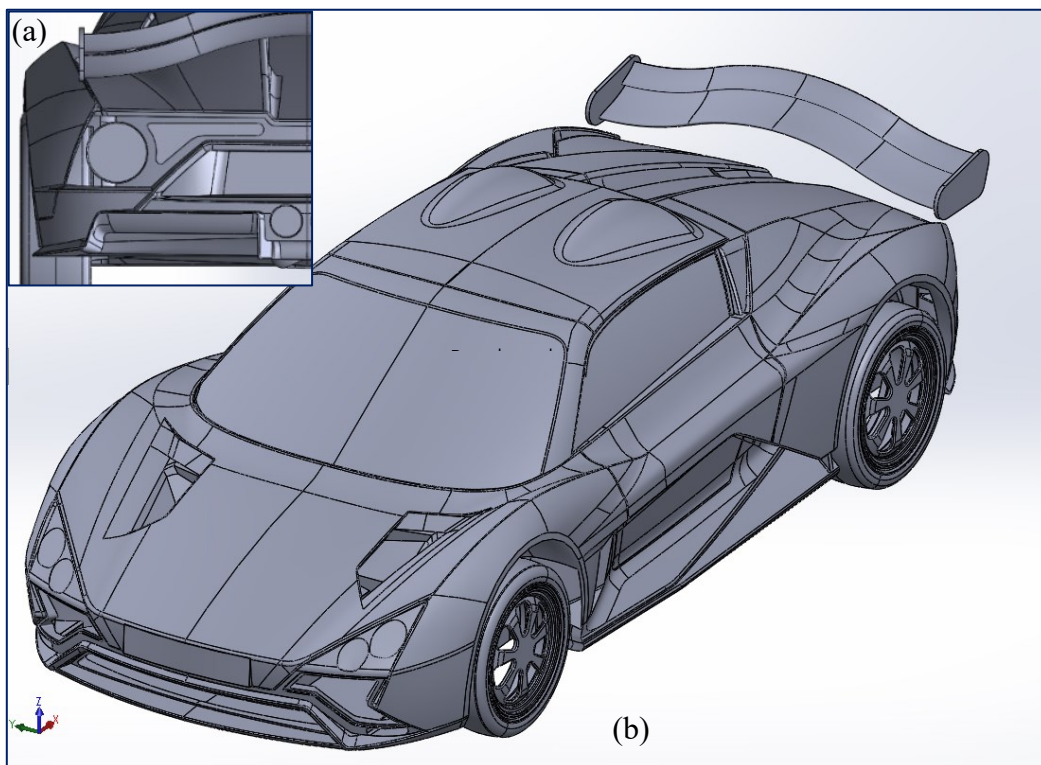

Figure 1. An illustration of the implemented car design for (a) left-half of rear-view and (b) 3D iso-view.

Wings with an optimised aerodynamic characteristic, in terms of aerofoil, generally contribute to a car's overall drag and lift performance. By conducting iterative CFD analysis initially on just the wing, time can be saved on subsequent whole vehicles CFD analyses (Chen *et al.*, 2011). Aerofoil S1223 (s1223-il) was selected to achieve

the required downforce at the rear side of the car. Different angles of attack were considered for each element (20° for main element and 35° for second element). The implemented wing design is shown in Figure 2.
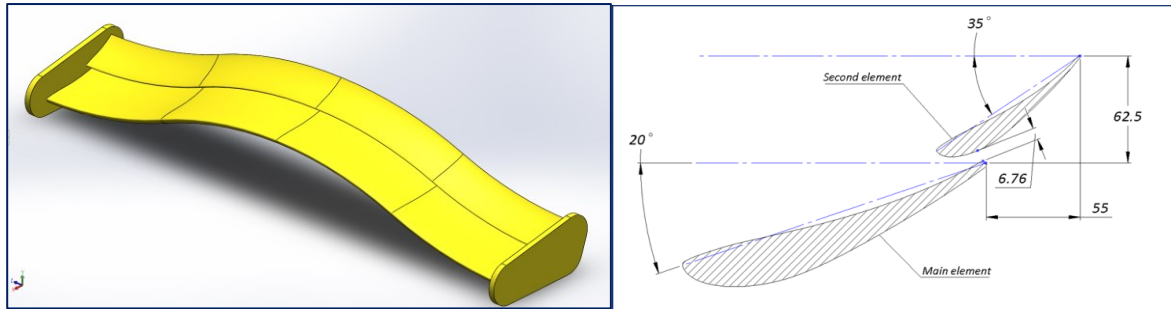

Figure 2. Double element wing and applied angle of attack.

For boundary conditions, the air inlet is set as "velocity inlet" with uniform flow, while the air outlet is set as "pressure outlet" with atmospheric pressure. In our analysis, the air inlet velocity for validation model is varied according to wind tunnel test, and the air velocity for actual car model is set as 40 m/s and 45 m/s. Trimmer cell is generated as the mesh element for the air medium and prism layer is only applied on the surface of the car and components (no prism layer on the wind tunnel wall). The wind tunnel walls are considered as smooth walls. Reynolds-Averaged Navier-Stroke equation (RANS) model is used for the simulation, with standard $k-\varepsilon$ turbulence model and turbulent viscosity, to solve the air flow. The air in the wind tunnel is considered at constant density. The time is advanced through a dual time-stepping implicit scheme. For the incompressible flow cases, the solver uses Rhie-Chow pressure-velocity coupling and SIMPLE algorithm. For the compressible solver, the inviscid fluxes are evaluated using the Weiss-Smith pre-conditioned Roe's flux difference splitting scheme. The two schemes are formally at best second order accurate. The viscous fluxes are evaluated by a standard central difference scheme. A second order central discretisation is used for both convective and diffusive terms. The convergence is conducted using residual values for RMS residual levels up to a maximum of 1E-4 for initial runs and down to 1E-6 for the verification case, which consumes longer computational time.

2.3 Meshing

A mix of tetrahedral, structure and prism elements were used to meet certain domain requirements. The mesh sizes and element types have been studied carefully with a mesh independence check of impact on solution (see Figure 3).
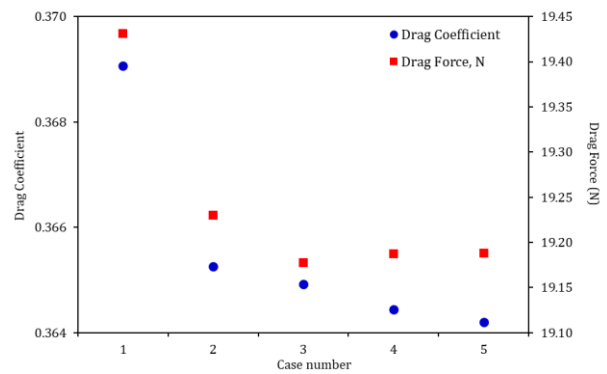
Figure 3. The impact of mesh sizing on predicted flow drag forces and coefficients. The cases (1–5) are provided in Table C1.

All simulations were solved for low Y+ values, in the range of 0 – 5 in the sub-viscous region. See Figure 4 for more illustration.
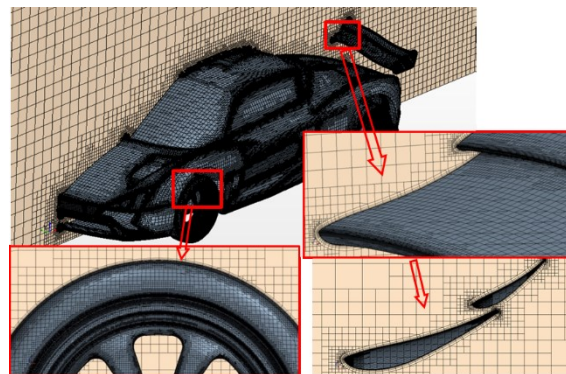
**Figure 4.** The boundary mesh of the fluid domain.

3. Results

Three benchmark models were constructed and simulated to set as the baseline for the improvement made in the later discussion. The results of the aerodynamic behaviour are shown in Table 2.

Table 2. The aerodynamic parameters used for the benchmark models (simulations are made at 40m/s wind speed).

Factor	Benchmark A - solid body (w/o wing)	Benchmark B - car with engine & components (w/o wing)	Benchmark C - car with engine, components & wing
C_D	0.368	0.379	0.377
C_L	0.280	0.215	0.032
Drag force (N)	603.040	621.398	634.200
Lift force (N)	451.380	352.499	54.410

In 'Benchmark A' model, the car model is totally solid. The purpose of simulating this model was to identify the high-pressure distribution areas for air intake, and also use it for simulations of modified models to save computational time as an original benchmark approach. In 'Benchmark B' model, the internal components of the benchmark design are accounted for, as shown in Figure 5. This model contains simplified models of chassis, radiator, and powertrain components in the compartments without the rear wing installed. In 'Benchmark model C', the Benchmark B is implemented with the rear wing attached. The rear wing design used in this model was designed at the initial project stage.
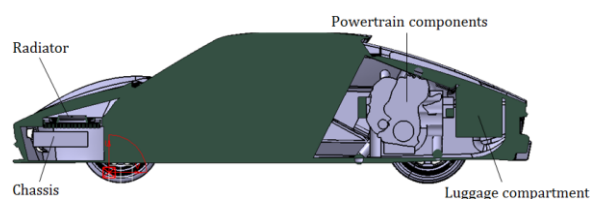
Figure 5. Benchmark B of a car model showing the engine and relevant internal-components without wing.

Considering the components inside the car profile slightly increased the drag coefficient by 3% comparing to totally solid model, which shows an opposite trend with Christoffersen's study on a Volvo S60 (Christoffersen *et al.*, 2010), but this might be due to the engine parts for the car is located at the rear of the car and the radiator is seated in front of the car, this has brought in a different behavioural trend to the car. However, the lift coefficient for the car has dropped crucially by 23% when the engine and other components are considered in this model. Undoubtingly, the addition of rear wing would further increase the drag but reduce in lift coefficient, yet, the impact is highly dependent on the design of rear wing. The design of the rear wing used in the simulation did not substantially affect the drag because it was hidden behind the car and the increase in frontal area was not particularly significant.

In Table 2, the drag forces are unacceptably high for a sports car. Also, the lift forces are found unbalanced between the front and rear axles in the benchmark models (illustrations are provided in Figures B.3, B5 – B7). There is a high lift force at rear axle of the car but high downforce acting on the front axle. This would cause poor stability when driving on road. Hence, improvement was required to increase the rear downforce, whilst considering the overall drag of the car.

3.1 Front Aerodynamics

The main objective for the development of the front part of the car was to reduce the drag and also locate the number plate in the appropriate position which did not adversely affect the drag characteristics.

3.1.1 Air curtains

Air curtains are small openings provided in the front of the car, usually below the head lamps or at the lower corners, in order to direct a free stream of air flow to pass from the opening and out again, in a way that it reduces the drag and aids fuel efficiency. In order to minimise drag without

extensive changes to the design of the car, an air curtain was implemented. This is shown in Appendix B (e.g., see Figure B4). The results obtained from the CFD simulation are shown in Figure 6, along with the comparison with the Benchmark model C results.

The air curtain was conceived considering the drag, whilst allowing more air flow towards the side ducts for the intercooler and the engine intake system. Due to this design modification, the drag was reduced by 10 counts. It also yielded a considerable influence on lift, reducing it by 12 counts. From the flow visualisation in Figure 6, it can be seen that, due to the air curtain, there was high velocity air flowing through the air curtain forcing air towards the wheel wells and the front side ducts. But also the flow was hitting the wheels. Hence the air curtain was slightly modified, as shown in Appendix B and the Support Material. Due to this modification a considerable further reduction in lift was observed.
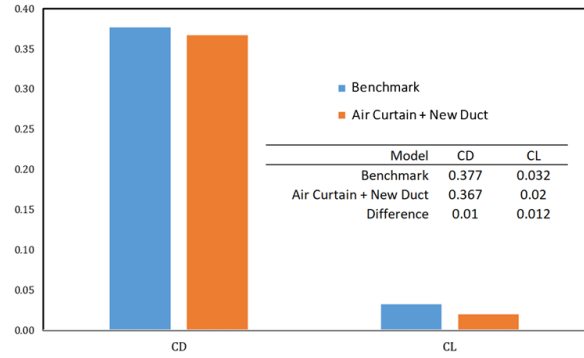
Figure 6. A CD and CL comparison chart between Benchmark C and our introduced air-curtain and new duct modification.

3.1.2 Number Plate Positioning

The number plate is placed near the nose of the car, as shown in Figure 7. A plinth is designed to change the angle of the plate, when viewed from the side of the car. A study has been made to choose the most appropriate location.
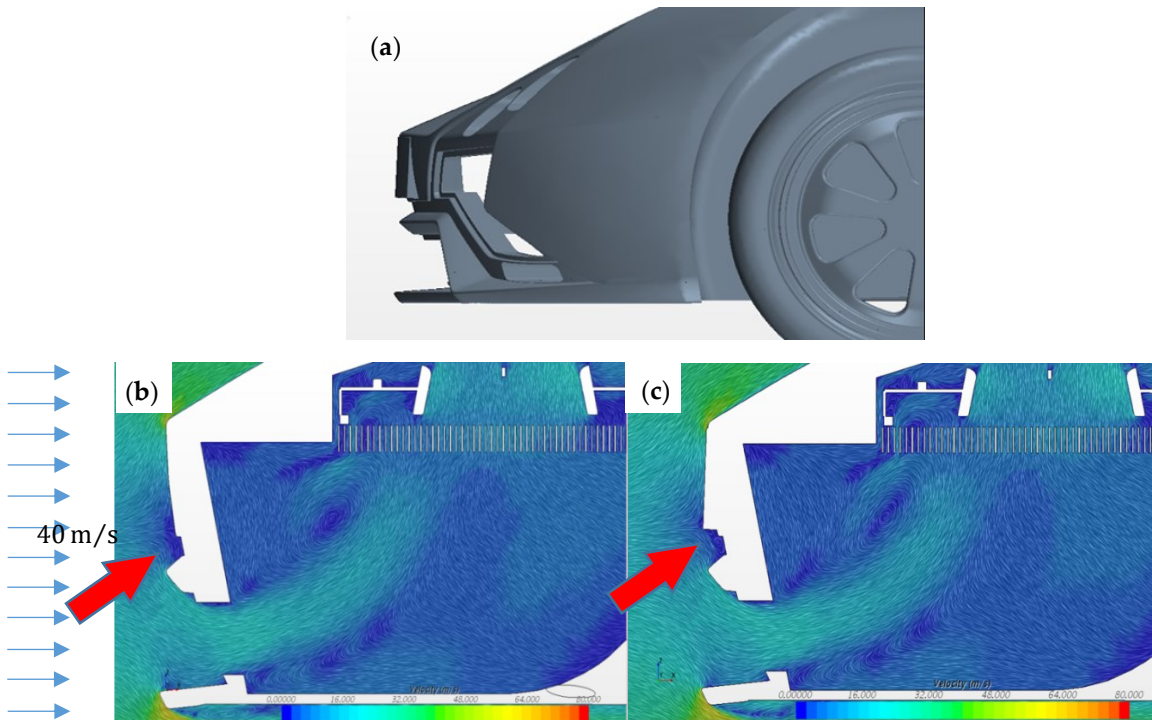

Figure 7. An illustration of (a) the side view of plate positioning, (b) the predicted air flow visualisation without a plate, and (c) the predicted air flow visualisation with a plate.

The position is found as the most convenient place to position the number plate. As a result, the low velocity air concentration has been reduced and distributed. In the given contours of velocity range, it is difficult to distinguish between the two cases (b and c) in Figure 7. The illustration of the positioning impacts on C_L and C_D is shown in Figure 8. It can be observed from Figure 8 that the drag is increased by 1 count as compared to the model

with only air curtain, accounting to a value of 0.368 for the entire car and a lift coefficient of 0.0082 due to the modified air curtain. Overall, due to the frontal development there has been a reduction of drag by 9 counts while also slightly being able to redirect the air more towards the side ducts. Based on this finding, there is some noticeable benefit in implementing the modified location of the number plate.
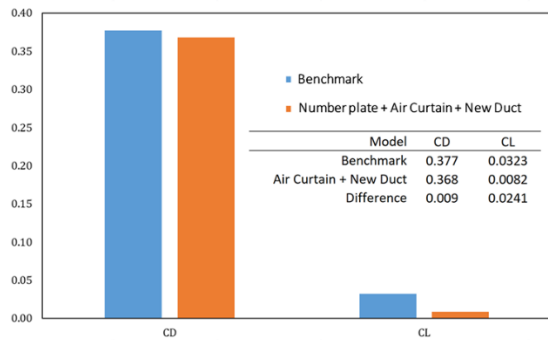
Figure 8. CD and CL comparison chart with number plate and air curtain.

## 3.2 Middle (Side) Aerodynamics

A range of design modifications were proposed, with the aim of directing air flow smoothly from the front to the rear of the car, with objective of reducing both drag and lift. Design concepts and the resulting objective results are shown in Figures 9–11. In the original (benchmark) design there was no front side duct. A front side duct was introduced and located behind the front wheel arch. This design was inspired by the findings from aerodynamic literature review, considering both sports and racing cars. Several design iterations of the front side duct were conducted and simulated to compare with "Benchmark A - Solid Body (w/o wing)".

The result of middle aerodynamic findings is presented in Table 3. The front side duct has improved both the drag and lift of the car. However, the improvement is not substantial. The maximum reduction in drag and lift coefficient is around 7 drag counts (1.9%) and 19 lift counts (6.8%) respectively.

Table 3. The effects front side duct on drag and lift forces and coefficients.[1]

| Design	Drag Coefficient	Drag Force (N)	Lift Coefficient	Lift Force (N)
Benchmark A – Solid body (without wing)	0.368	761.100	0.280	580.794
Front Side Duct Design–1	0.366	760.700	0.276	572.900
Front Side Duct Design–2	0.362	750.760	0.273	567.000
Front Side Duct Design–2 & Stopper	0.361	749.730	0.261	542.300

[1] All simulations were made at wind speed 45 m/s.
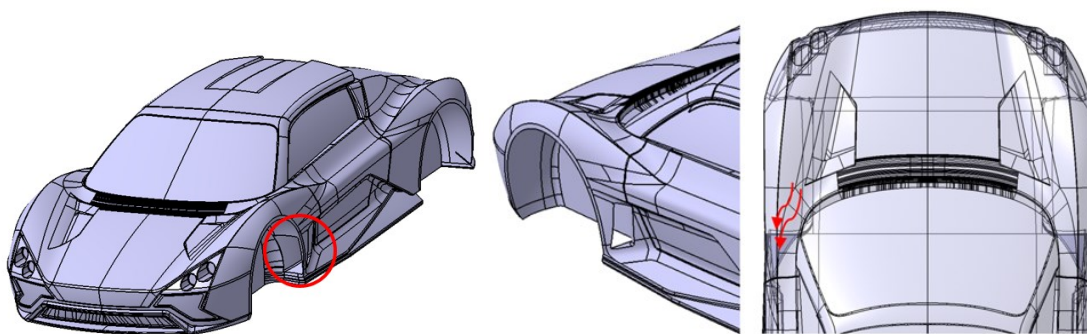
Figure 9. Front side duct design 1 (left: view from the back, right: transparent view from top).

The second design of the front side duct, shown in Figure 10, yields an improvement compared to the first design. The wider opening of the duct at the front wheel arch allows less restricted air flowing and the profile of the duct, running almost tangentially to the inner flat surface of wheel arch. This has created a smoother air flow path. Fins are added in the duct with an angle of -1 degree from the ground plane with the intention of directing air to the intake ducts for engine and intercooler.
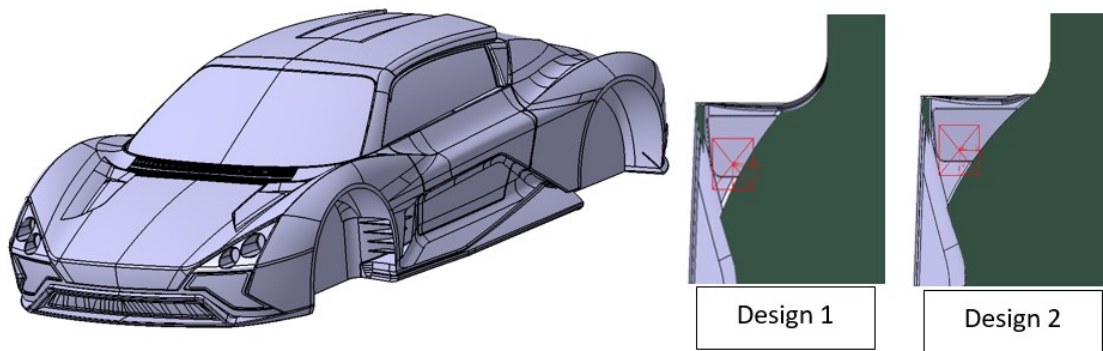

Figure 10. Left - design for front side duct 2, right - profile of duct in cross-section view.

As an observation from the pressure distribution around the car with front side duct design 1, the side profile design behind the door allows some air to escape from the air intake area. It constantly hits the rear wheels and creates high pressure zone, as illustrated in Figure 11. This can be observed at the wheel surface in the direction of air leakage from the car body (see Appendix B). This condition would have resulted in negative effect to aerodynamic performance. To address this issue, a stopper under the air intake is created to merge with the car body and the aerodynamic effect was observed (on model with front side duct, Design 2). The stopper is located under the air intake behind the door and in front of the rear wheel. The purpose of the stopper is to cover up the hole in the benchmark model and direct more air towards the engine air intake and intercooler radiator. Additionally, the stopper has prevented air from escaping towards the rear wheel. The results show improvement in drag and lift coefficient for both design concepts.

It has been noticed that adding the fins in design 2 does not give an ideal result, the air is found to be swirling in between the fins and is non-uniform, which creates drag. Looking at the pressure distribution in Appendix B, the front side duct design 1 improves the pressure inlet at the air intake surface by increment of around 8 Pa, but the side duct design 2 reacts oppositely, the pressure has dropped severely to around 200 Pa, compared to the pressure of 316 Pa on benchmark model, this has proven that addition of fins in the duct does not help in directing the air from the wheel arch to the air intake area. A final design for front side duct was created according to design 2 but without the fins to verify the performance, more improvement on drag and lift coefficient has been shown as compared to model with fins, as illustrated in Table 4. The flow within the duct is smooth without air circulation.
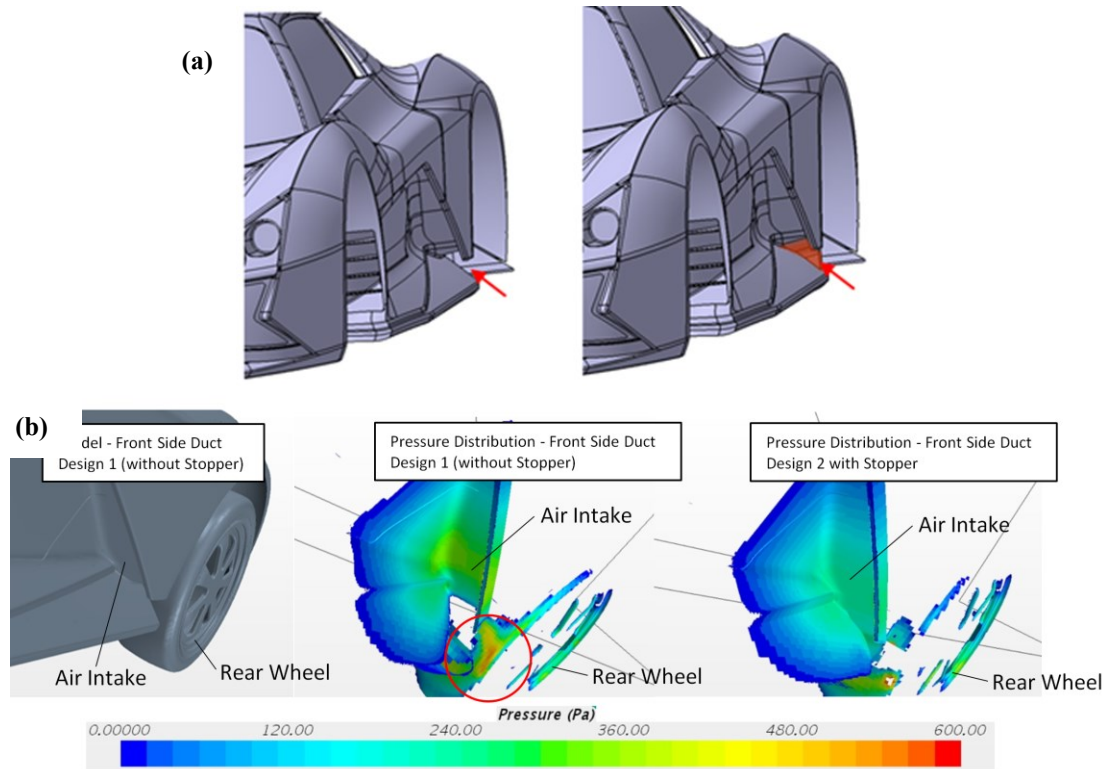
Figure 11. The stopper gate under the air intake (a) and effected pressure distribution (b).

Table 4. Improvement Made by Front Side Duct 2 (without Fins) + Stopper. [1]

Design	Drag Coefficient, C_d		Drag Force (N)	Lift Coefficient, C_L		Lift Force (N)
	Value	Improvement %	Value	Value	Improvement %	Value
Benchmark A – solid body (without wing)	0.368	-	761.100	0.280	-	580.794
Front side duct design-2 (without fins) + stopper	0.341	7.337	707.140	0.186	33.500	386.620

[1] All simulations were made at wind speed 45 m/s.

3.3 Rear Aerodynamic Development

3.3.1. Roof Curvature and height

The original design of roof drove high velocity air away from the rear wing; this led to less downforce being produced by the wing. Another issue was that some vortices were generated behind the roof, which created a weak flow in that area. As a result, the optimum downforce which could have been achieved was not being generated by the rear wing Figure 12.
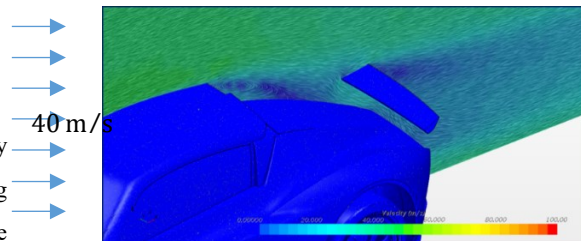

Figure 12. Weak flow direction and velocity contours behind original roof.

40 m/s

To overcome these issues with the roof shape, a new design was conceived to drive more flow to the wing location. A further benefit was that the aesthetics were improved. During the roof re-design process two dome shapes were added to provide head clearance for the occupants.

For detailed vision of the reduction of vortices behind the roof due to the new roof design see Appendix B. It was also demonstrated that the new wing experienced higher velocity air comparing with the original design. In addition, the new roof design kept the flow attached to body and drag reduced by 1.13%, while downforce increased by 2.23% (see Figures 13 and 14).
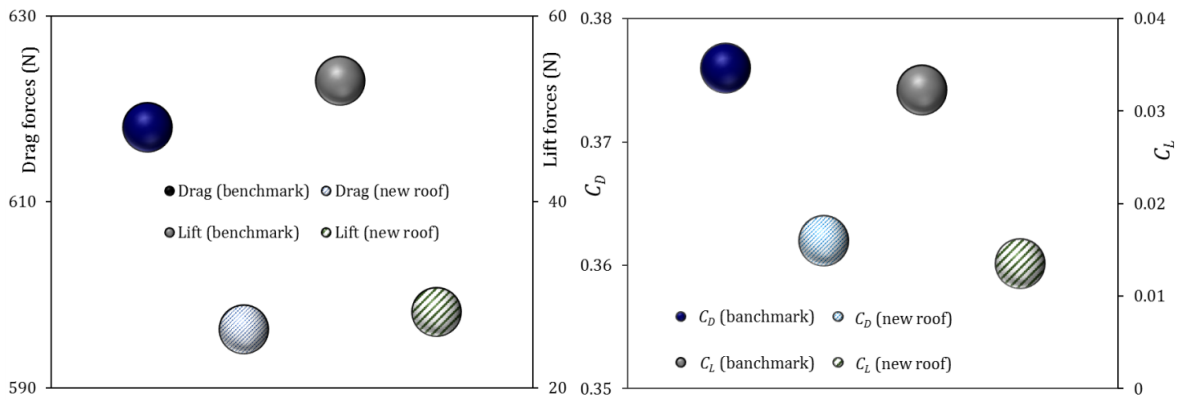
Figure 13. Impact of the new roof design on (a) drag and lift forces and (b) coefficients.
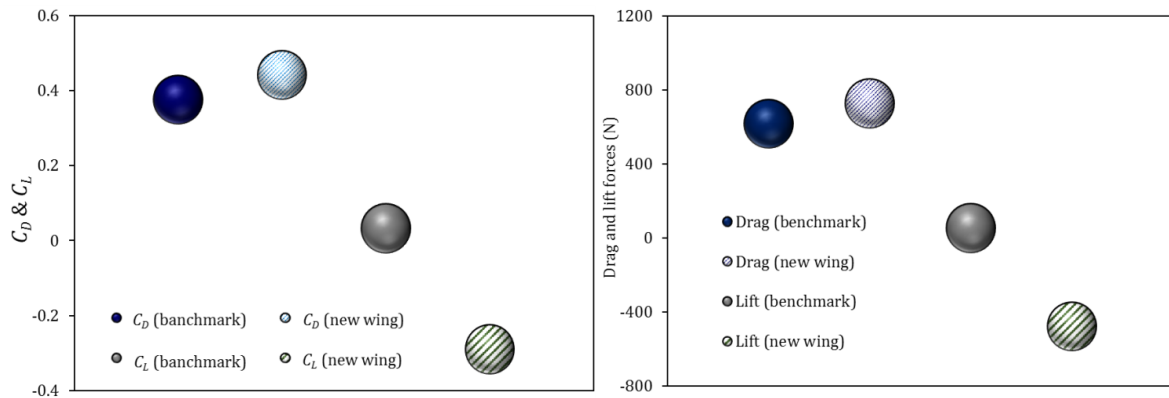
Figure 14. Impacts of the new wing on (a) drag and lift forces, and (a) coefficients.

3.3.3. Rear wing spoiler design characteristics

According to (Buljac *et al.*, 2016), the lift coefficient C_L reaches the maximum at certain angle of attack (depending on air foil), and no more increase in lift coefficient even with increase of angle (practically C_L decrease). However, the drag coefficient C_D increases with an increase in angle of attack (Pugliese *et al.*, 2013; Buljac *et al.*, 2016; Das & Riyad, 2017).

Rear wing play a significant role in drag and lift forces (Fukuda, 1995). As shown by Howell & Le Good (1999), the required downforce with an acceptable level of drag can be achie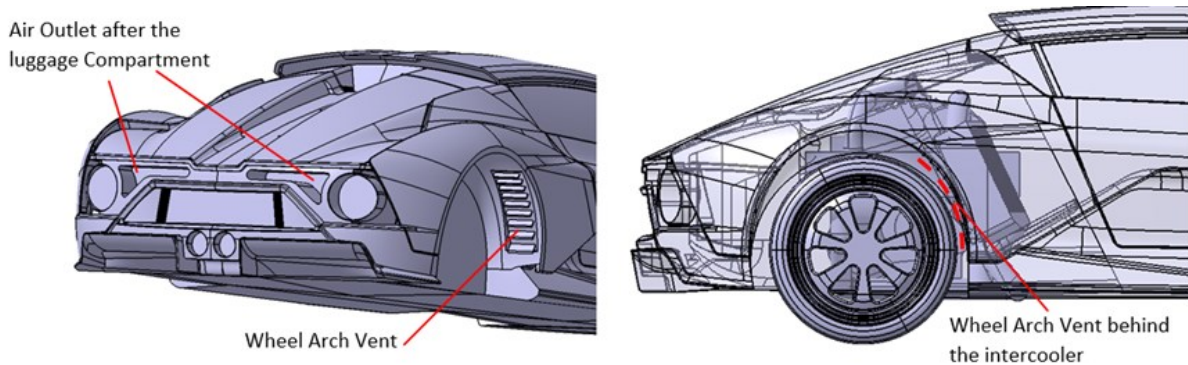ved by selecting the optimum parameters, such as aerofoil and angle of attack, which leads to better stability during acceleration, turning and maneuver. Also, Howell and Le Good (1999) pointed out that rear axle lift is a common concern for aerodynamics, as a result of the basic shape of a car. A number of rear spoiler configurations in various locations were recommended during their study to increase rear axle downforce.

The shape of wing was re-designed to maximize downforce, taking into account the drag force at the same time. Figure B8 (Appendix B) shows the high velocity at the sides of the car body. This led to a curved wing (double element) design with more height in the middle (~ 136.0

mm) to catch the air stream above the roof and at the sides of the body.

3.3.4. Ducts and Vents

In addition to using ducts for cooling purposes, high performance sports cars are also equipped with ducting and vent designs that allow air flow at critical locations, in order to reduce the drag and lift on the car. Three main changes were made to the middle and rear of the car that predicted to improve aerodynamic performance. The first

change made was to fix a vent at the front side of the rear wheel arch. The two reasons for this change were; firstly, to allow the air passing through the intercooler to have direct exit to atmosphere, preventing the air hitting the wheel arch. Secondly, to allow the hot air passed from the drivetrain to exit from the engine compartment. The vent was shielded by fins to prevent mud and road debris blocking the intercooler when the car is driven on the road. The design is shown in Figure 15.

Figure 15. Wheel arch vent and air outlet at rear.

As can be seen from Figure 15, an additional air outlet from the engine compartment was created behind the luggage compartment (beside the tail light) to allow more air to escape from the engine bay. It was assumed that the engine compartment required free flowing to allow facilitate powertrain cooling. A channel between the rear end of the car and luggage compartment allows air to escape. The third design change applied at the rear of the car was to create an air passage behind the rear wheel arch, shown in Figure 16.
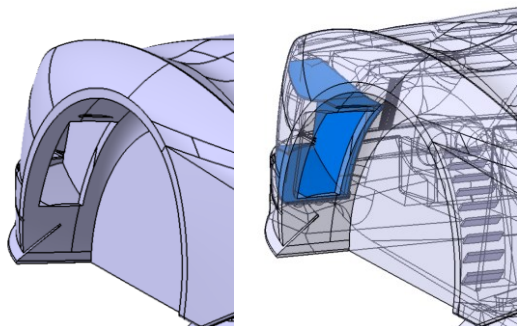
Figure 16. The ducting created behind the rear wheel arch.

A duct was designed to create this air passage. This design used the air outlet located at the side of the tail light as the exit of the duct. Hot air from the engine bay is bled into the rear wheel housing and the rear duct serves the purpose of venting this heat.

The analysis was carried out by adding one design change per simulation to evaluate the contribution of each design modification to the aerodynamic performance. The changes of the car were made on the "Benchmark B - Car with engine and components (w/o rear wing)" model and results compared against this benchmark. It should be emphasized that both, left and right (RHS), hand sides of the vehicle are almost identical, but the the components under the RHS of car have slightly more detailed intercooler components. We assumed a symmetrical body to minimise the computational time, and the RHS of the car model was chosen for simulation. The summary of the result is shown in Table 5.

Table 5. The effects of rear aerodynamic design optimisation on drag and lift forces and coefficients.[1]

Design	Drag Coefficient, C_D	Drag Force (N)	Lift Coefficient, C_L	Lift Force (N)
Benchmark B - car with engine & components (w/o wing)	0.379	621.398	0.215	352.499
Including intercooler vent	0.370	606.800	0.197	323.550
Including intercooler vent & rear air outlet	0.376	616.840	0.243	398.371
Including intercooler vent, rear air outlet & rear wheel arch duct	0.366	600.256	0.190	312.200

In general, applying the design changes reduce both drag and the lift coefficient. For the final outcome, the drag and lift coefficients has dropped to 0.366 and 0.190, respectively, compared to Benchmark B model result with $C_D = 0.379$ and $C_L = 0.215$ (reduced 3.4% in drag coefficient and 11.6% in lift coefficient). The reduction in drag coefficient is expected because the creation of duct behind the wheel allows a largely unrestricted air flow path from the intercooler vent to rear wheel arch. The flow then exits through the back of the car via the rear wheel arch duct, as illustrated in Appendix B (see Figure B6).

As one can see from the results, adding an air outlet at the rear end of the car does not provide an ideal result for the drag and lift coefficient of the car. The drag increases by 6 drag counts compared to the model with only an intercooler vent and the lift coefficient has risen to 0.243, i.e. 13% more than the benchmark model. The increase in drag force

at the rear compartment is due to the narrow air passage in between the luggage compartment and rear end of the car. The pathway for the air to exit from the engine compartment (see illustrations in Appendix B) is tortuous and causes a wide variation in air speed within the path. Although the rear end air outlet car does not introduce noticeable benefits to the aerodynamic performance, it is needed to allow hot air from engine compartment to escape into the atmosphere. The transient contours of the simulation are also available as supplementary video clips.

3.3.5 Final integrated model

Final modifications and solutions were merged to carry out a final simulation, and improvements were added, as shown in Appendix B (Figure B9). The difference between benchmark and integrated design result are shown in Table 6.

Table 6. A comparison among benchmark, improved and integrated designs for drag and lift forces and coefficients.

Designs type	C_D	Drag force (N)	C_L	Downforce (N)	L/D
Benchmark C	0.376	618.02	0.0323	-53.02	0.085
Improved	0.441	727.56	-0.29	478.65	0.657
Integrated	0.438	721.13	-0.343	566.18	0.785

Considering aforementioned results, it can be observed that by merging all modifications, the C_D has increased by $\triangle C_D = 0.062$ (↑16.49 %) but C_L has improved by $\triangle C_L = -0.3753$ (↑1161.92 %) compared to the Benchmark C. More details regarding the difference between Benchmark

C and the integrated design (with all modifications merged) can be seen in Appendix D.

3.4 Validation

Wind tunnel and CFD simulations contribute to aerodynamic development is different ways. Wind tunnel

work helps in fine-tuning of designs and final validation; whereas CFD simulations can be used to swiftly assess different configurations at various design points. As far as realistic flow fields are concerned neither the wind tunnel nor CFD simulations are perfectly accurate. But accuracy of results has improved over the decades. The comparison of results obtained between the wind tunnel and CFD simulations are interpreted graphically, as shown in Figure 17 for the drag and lift forces and coefficients.
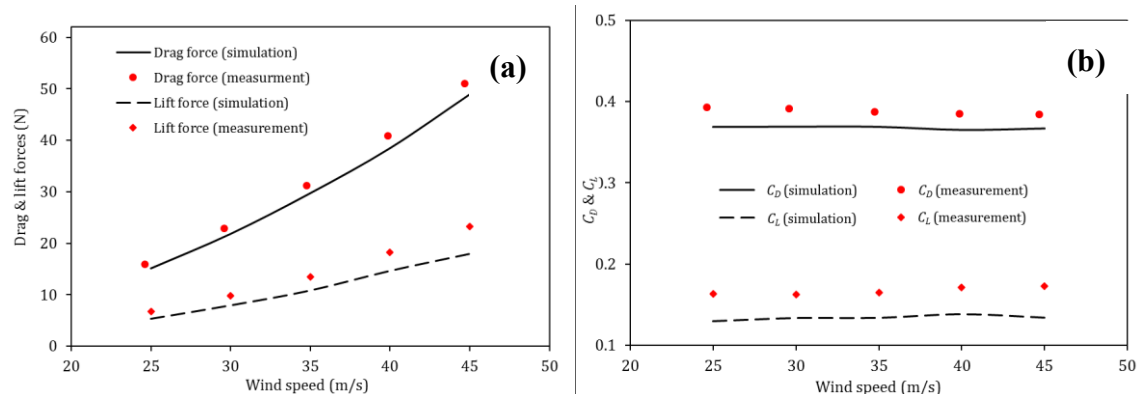
Figure 17. Wind tunnel measured and CFD simulated drag and lift (a) forces and (b) coefficients versus wind speed.

It is observed that there is slight variation between the obtained results of drag from wind tunnel and simulation results. The difference is not beyond 40 drag counts (0.040) at any speeds from 25 to 45 m/s, with an average error percentage of 4% to 24%. The percentage error becomes significant for small lift (almost negligible) forces although the deviation value is insignificant (≤ 5 N). The graphs indicate that there are similar trends for results obtained for both the wind tunnel as well as CFD simulations for the lift aspect of the car. Key aerodynamic simulations are also available as supplementary videos.

4. Conclusion

The overall aerodynamic development of the lightweight sports car combined of both, theoretical modelling and physical tests, has been demonstrated. This work substantially improved the basic aerodynamic characteristics of the car and has provided a sound base for further development based on full scale testing. A key requirement was to increase rear end downforce to benefit stability and safety. This has been achieved whilst not substantially affecting the drag coefficient. Inevitably, increased downforce does result in extra drag. The car now possesses a C_D value of 0.438 but it can be said that the car is much stable and more balanced compared to the benchmark C model, due to the high downforce of 566N at

40 m/s wind speed. The new roof design has kept the flow attached to body and has reduced drag by 1.13 %, while downforce has increased by 2.23 % compared with the Benchmark C. Although the individual modifications of the frontal and side parts of the car brought down the drag around 9 and 13 counts respectively, their implementation along with the new rear wing (integrated model) has helped in slightly reducing the overall drag by 3 counts, at the same time improve the overall downforce (Appendix B).

REFERENCES

AHMED, S.R., GAWTHORPE, R.G., & MACKRODT, P.-A. (1985) Aerodynamics of Road- and Rail Vehicles. *Vehicle System Dynamics*, **14**, 319–392.

BULJAC, A., DŽIJAN, I., KORADE, I., KRIZMANIĆ, S., & KOZMAR, H. (2016) Automobile aerodynamics influenced by airfoil-shaped rear wing. *International Journal of Automotive Technology*, **17**, 377–385.

BUSCARIOLO, F.F. & KARBON, K.J. (2011) Comparative CFD Analysis Between Rotating and Static Cases of Different Wheels Opening Designs over a Performance Sedan.

CHEN, M.N., TANG, W.H., YANG, B., & HU, X.J. (2011) Computer-Aided Front and Rear Wings Aerodynamic

Design of a Formula SAE Racing Car. *Applied Mechanics and Materials*, **120**, 20–25.

CHRISTOFFERSEN, L., LÖFDAHL, L., & JÖNSON, A. (2010) Interference between Engine Bay Flow and External Aerodynamics of Road Vehicles.

DAS, R.C. & RIYAD, M. (2017) CFD Analysis of Passenger Vehicleat Various Angle of Rear End Spoiler. *Procedia Engineering*, **194**, 160–165.

FUKUDA, H. (1995) Improvement of vehicle aerodynamics by wake control. *JSAE Review*, **16**, 151–155.

GOETZ, H. (1971) The Influence of Wind Tunnel Tests on Body Design, Ventilation, and Surface Deposits of Sedans and Sport Cars.

HAN, Y., CAI, C.S., ZHANG, J., CHEN, S., & HE, X. (2014) Effects of aerodynamic parameters on the dynamic responses of road vehicles and bridges under cross winds. *Journal of Wind Engineering and Industrial Aerodynamics*, **134**, 78–95.

HASSAN, S.M.R., ISLAM, T., ALI, M., & ISLAM, M.Q. (2014) Numerical Study on Aerodynamic Drag Reduction of Racing Cars. *Procedia Engineering*, **90**, 308–313.

HOWELL, J. & LE GOOD, G. (1999) The Influence of Aerodynamic Lift on High Speed Stability.

HUCHO, W.-H. & AERODYNAMIK (1987) *Aerodynamics of road vehicles: from fluid mechanics to vehicle engineering.*

HUMINIC, A. & HUMINIC, G. (2008) On the Aerodynamics of the Racing Cars.

HUMINIC, A., HUMINIC, G., & SOICA, A. (2012) Study of aerodynamics for a simplified car model with the underbody shaped as a Venturi nozzle. *International Journal of Vehicle Design*, **58**, 15.

KATZ, J. (2006) AERODYNAMICS OF RACE CARS. *Annual Review of Fluid Mechanics*, **38**, 27–63.

KHALED, M., EL HAGE, H., HARAMBAT, F., & PEERHOSSAINI, H. (2012) Some innovative concepts for car drag reduction: A parametric analysis of aerodynamic forces on a simplified body. *Journal of Wind Engineering and Industrial Aerodynamics*, **107**–**108**, 36–47.

KODIYALAM, S. & SOBIESZCZANSKI-SOBIESKI, J. (2001) Multidisciplinary design optimisation - some formal methods, framework requirements, and application to vehicle design. *International Journal of Vehicle Design*, **25**, 3.

KOITRAND, S., LOFDAHL, L., REHNBERG, S., & GAYLARD, A. (2014) A Computational Investigation of Ground Simulation for a Saloon Car. *SAE International Journal of Commercial Vehicles*, **7**, 111–123.

MARCHESIN, F.P., BARBOSA, R.S., GADOLA, M., & CHINDAMO, D. (2017) High downforce race car vertical dynamics: aerodynamic index. *Vehicle System Dynamics*, 1–20.

MOHRFELD-HALTERMAN, J.A. & UDDIN, M. (2016a) Quasi steady-state aerodynamic model development for race vehicle simulations. *Vehicle System Dynamics*, **54**, 124–136.

MOHRFELD-HALTERMAN, J.A. & UDDIN, M. (2016b) High fidelity quasi steady-state aerodynamic model effects on race vehicle performance predictions using multi-body simulation. *Vehicle System Dynamics*, **54**, 963–981.

PIROZZOLI, S. (2018) On turbulent friction in straight ducts with complex cross-section: the wall law and the hydraulic diameter. *Journal of Fluid Mechanics*, **846**.

PUGLIESE, A., YANG, Z.G., & LI, Q.L. (2013) CFD Research and Investigation of 2011 P4/5 Competition Rear Wing. *Applied Mechanics and Materials*, **275**–**277**, 665–671.

RAO, J.S., SARAVANAKUMAR, M., & CHANDAR, D.C.V. (2007) External Aerodynamic Flow for High Speed Passenger Car.

ROAD VEHICLE AERODYNAMICS FORUM COMMITTEE (1994) Aerodynamic Testing of Road Vehicles – Open Throat Wind Tunnel Adjustment (An American National Standard No. J20J2071_199406). SAE, USA.

SADEGHIZADEH, M., SHIRAZ, SARANJAM, B., SHIRAZ UNIVERSITY, KAMALI, R., & SHIRAZ UNIVERSITY (2017) Experimental and Numerical Investigation of Drag Force at High Speed Diver Motion in Different Depths from Free Surface. *Journal of Applied Fluid Mechanics*, **10**, 343–352.

SKINNER, S.N. & ZARE-BEHTASH, H. (2018) State-of-the-art in aerodynamic shape optimisation methods. *Applied Soft Computing*, **62**, 933–962.

TSAI, C.-H., FU, L.-M., TAI, C.-H., HUANG, Y.-L., & LEONG, J.-C. (2009) Computational aero-acoustic analysis of a passenger car with a rear spoiler. *Applied Mathematical Modelling*, **33**, 3661–3673.

YANG, W., DENG, E., LEI, M., ZHANG, P., & YIN, R. (2018) Flow structure and aerodynamic behavior evolution during train entering tunnel with entrance in crosswind. *Journal of Wind Engineering and Industrial Aerodynamics*, **175**, 229–243.

ZHANG, J., WANG, J., WANG, Q., XIONG, X., & GAO, G. (2018) A study of the influence of bogie cut outs' angles on the aerodynamic performance of a high-speed train. *Journal of Wind Engineering and Industrial Aerodynamics*, **175**, 153–168.

Appendix A. Governing equations

The main governing equations solved numerically using StarCCM+ (Commercial CFD package) are provided in this appendix.

Continuity Equation (Steady, 3-D, incompressible)

$$\partial \rho / \partial t + \nabla \cdot (\rho \vec{V}) = 0,$$

where ρ is the scalar density, t is time, and $\vec{V}$ is the vector velocity field.

Momentum Equation

$$x - component: \frac{\partial(\rho u)}{\partial t} + \nabla \cdot (\rho u \vec{V}) = -\frac{\partial p}{\partial x} + \frac{\partial \tau_{xx}}{\partial x} + \frac{\partial \tau_{yx}}{\partial y} + \frac{\partial \tau_{zx}}{\partial z} + \rho f_x,$$

$$y - component: \frac{\partial(\rho v)}{\partial t} + \nabla \cdot (\rho v \vec{V}) = -\frac{\partial p}{\partial y} + \frac{\partial \tau_{xy}}{\partial x} + \frac{\partial \tau_{yy}}{\partial y} + \frac{\partial \tau_{zy}}{\partial z} + \rho f_y,$$

$$z - component: \frac{\partial(\rho w)}{\partial t} + \nabla \cdot (\rho w \vec{V}) = -\frac{\partial p}{\partial z} + \frac{\partial \tau_{xz}}{\partial x} + \frac{\partial \tau_{yz}}{\partial y} + \frac{\partial \tau_{zz}}{\partial z} + \rho f_z,$$

where τ is the shear stress (in Pa), f is the body force per unit mass, and the velocity for component x, y, and z are given respectively with $u = u(x, y, z, t)$, $v = v(x, y, z, t)$, and $w = w(x, y, z, t)$.

Viscous force can be related to the fluid deformation

$$\sigma_{xx} = -p + \tau_{xx}, \ \sigma_{yy} = -p + \tau_{yy}, \ \sigma_{zz} = -p + \tau_{zz}.$$

Conservation of Angular Momentum

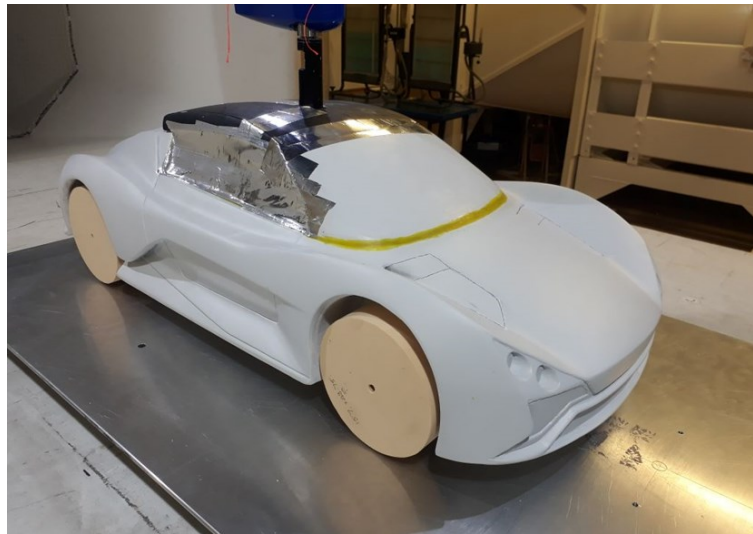Conservation of angular momentum requires that the stress tensor is symmetric: $\sigma = \sigma^{\mathrm{T}}$.

Energy Equation

$$\frac{\partial}{\partial t}\left[\rho\left(e + \frac{v^2}{2}\right)\right] + \nabla \cdot \left[\rho\left(e + \frac{V^2}{2}\vec{V}\right)\right] = \rho\dot{q} + \frac{\partial}{\partial x}\left(k\frac{\delta T}{\delta x}\right) + \frac{\partial}{\partial y}\left(k\frac{\partial T}{\partial y}\right) + \frac{\partial}{\partial z}\left(k\frac{\partial T}{\partial z}\right) - \frac{\partial(up)}{\partial x} - \frac{\partial(vp)}{\partial y} - \frac{\partial(wp)}{\partial z} + \frac{\partial(u\tau_{xx})}{\partial x} +$$
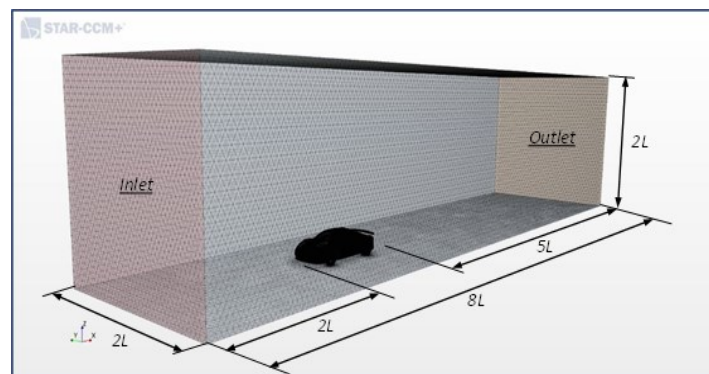
$$\frac{\partial(u\tau_{yx})}{\partial y} + \frac{\partial(u\tau_{zx})}{\partial z} + \frac{\partial(v\tau_{xy})}{\partial x} + \frac{\partial(v\tau_{yy})}{\partial y} + \frac{\partial(v\tau_{zy})}{\partial z} + \frac{\partial(w\tau_{xz})}{\partial x} + \frac{\partial(w\tau_{yz})}{\partial y} + \frac{\partial(w\tau_{zz})}{\partial z} + \rho\vec{f}\cdot\vec{V}$$

where V is control volume, $\left(e + \frac{v^2}{2}\right)$ is the total energy, k is the thermal conduction ($\mathrm{W}m^{-1}\mathrm{K}^{-1}$), T is the temperature (K).

Appendix B. Model optimisation

Figure B1. The 1/4 scale prototype used in our wind tunnel experiment.


Figure B2. The wind tunnel size for a full scale car model.

**Table B1.** The mesh refinement cases tested for a mesh independence check.

Location	Mesh refinement cases	1	2	3	4	5
Body without Wing	Base Size (mm)	200	100	100	100	95
	Min. Surface Size (%)	10	5	5	2.5	5
	Surface Curvature	36	36	36	36	36
	Surface Growth Rate	1.3	1.3	1.3	1.3	1.3
	Number of Prism Layers	18	18	18	18	18
	Prism Layer Stretching	1.8	1.8	1.8	1.8	1.8
	Prism Layer Total Thickness	0.5	0.5	0.5	0.5	0.5
Al Board	Target Surface Size (%)	40	20	10	10	10
	Minimum Surface Size (%)	1	0.5	0.25	0.25	0.25
	Surface Growth Rate	1.5	1.5	1.5	1.5	1.5
	Target Surface Size	40	20	10	10	10

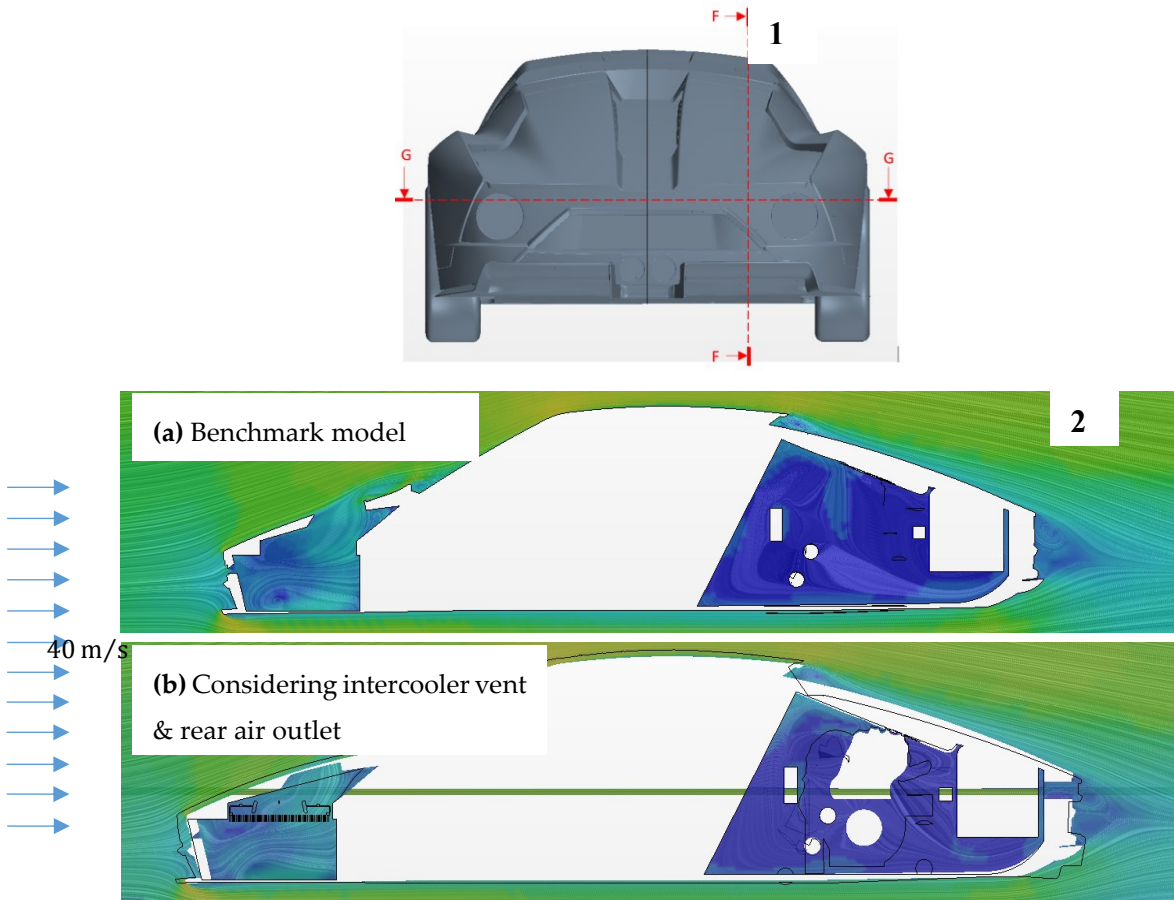|						
Car Body	Minimum Surface Size (%)	1	0.5	0.25	0.25	0.25
	Surface Curvature	72	72	72	72	72
	Surface Growth Rate	1.5	1.5	1.5	1.5	1.5
Wheels	Target Surface Size	50	50	50	50	50
	Minimum Surface Size (%)	2.5	2.5	2.5	2.5	2.5
Wing	Cells no.	845962	3481953	6340008	6339096	6438146
	Faces no.	2529225	10417962	18989700	18987583	20177082
	Vertices no.	934240	3812185	6948051	6947944	7381244
	Drag Coefficient	0.3691	0.3653	0.3649	0.3644	0.3642
	Drag Force (N)	19.4311	19.2303	19.1777	19.1874	19.1883
	Lift Coefficient	0.1663	0.1511	0.1629	0.1534	0.15308
	Lift Force (N)	8.7535	7.9551	8.6140	8.0780	8.0847
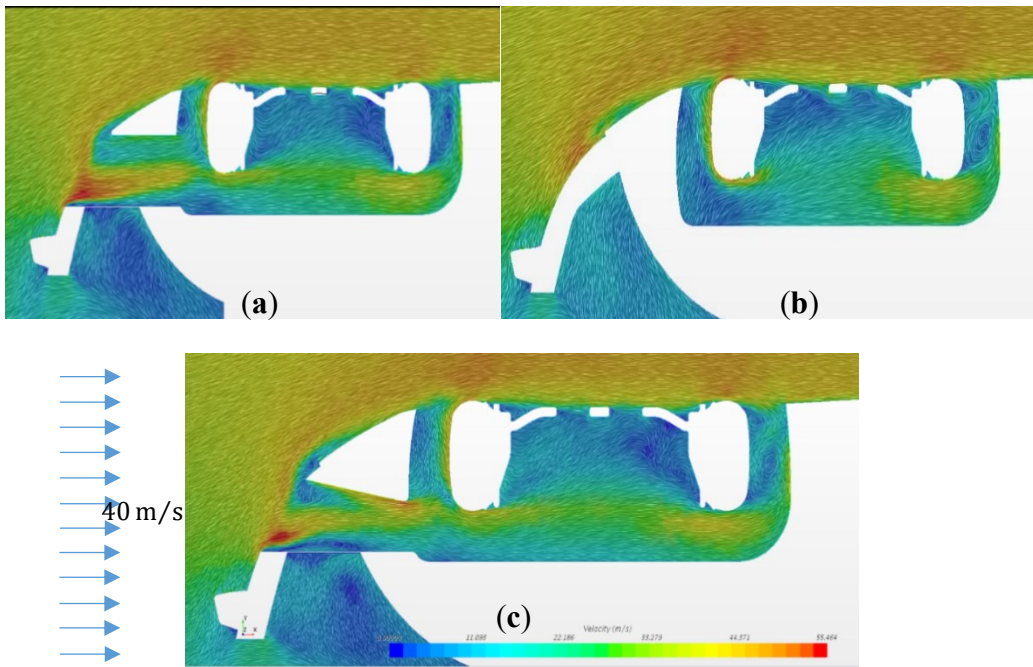
Figure B3. Flow visualisation through the side-intercooling ducts (**a**) with air curtain, (**b**) without air curtain, and (**c**) with a modified air curtain.
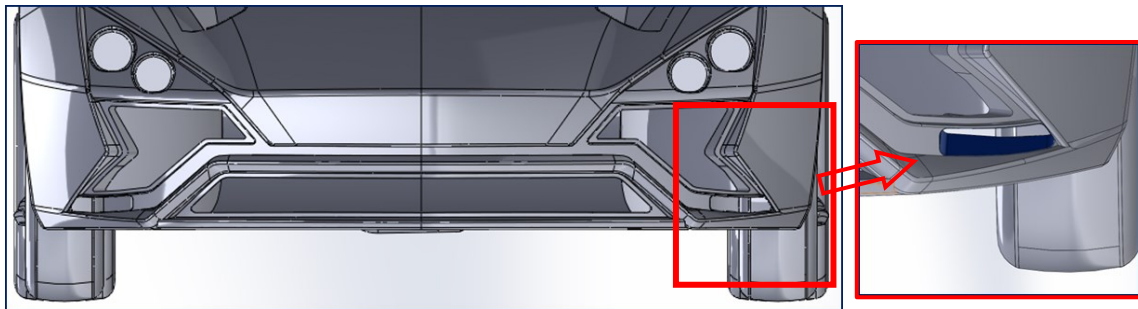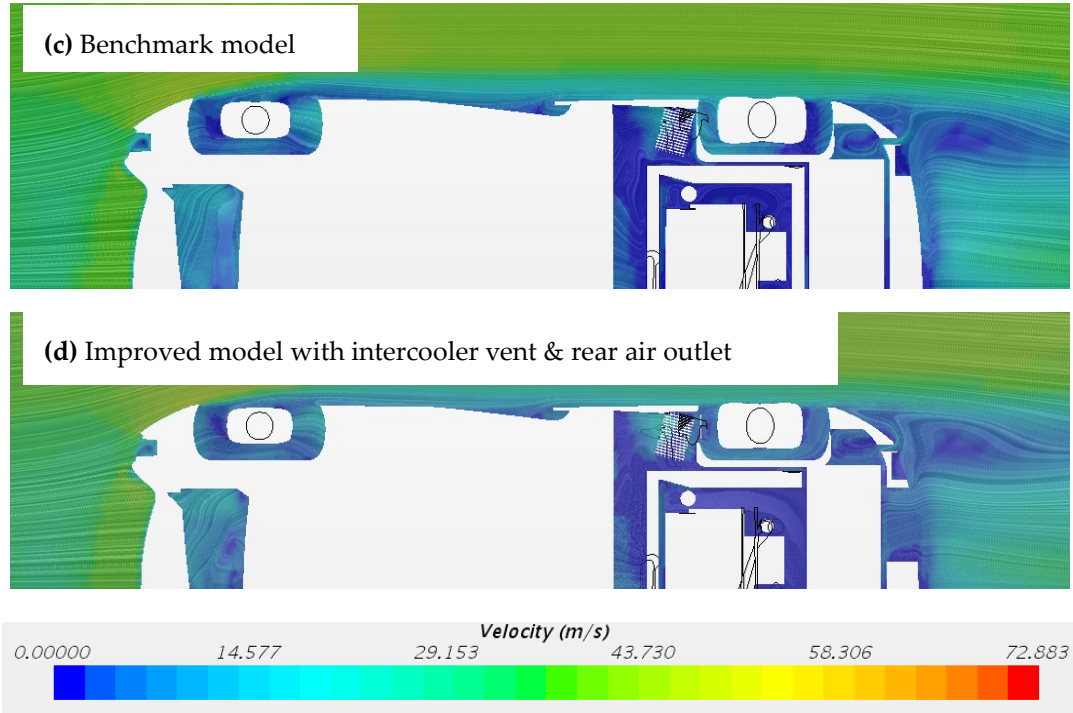

**Figure B4. The introduced air curtain design.**
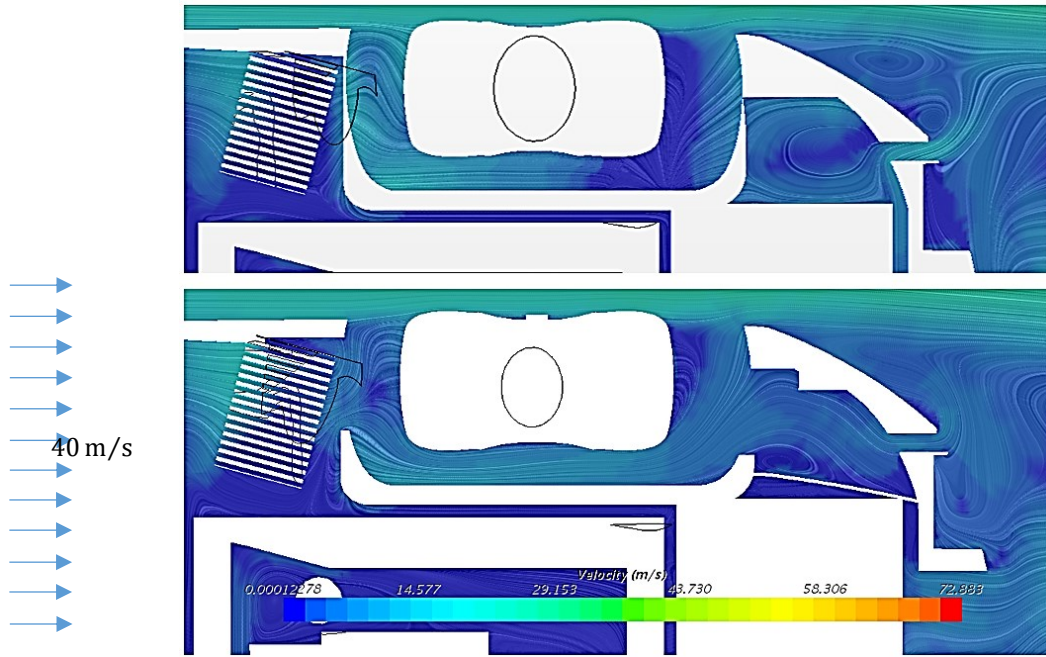
Figure B5. Air flow in rear wheel arch (top: benchmark model, bottom: model with intercooler vent, rear car air outlet and rear wheel arch duct).

(c) Benchmark model

(d) Improved model with intercooler vent & rear air outlet

Velocity (m/s)

| 0.00000 | 14.577 | 29.153 | 43.730 | 58.306 | 72.883 |

Figure B6. Diagrams of 1. A schematic of the vehicle showing the cross section locations; and 2. Airflow by cross-section, in side view with illustration of F-F cross section of (a) benchmarck B and (b) improved models, and G-G cross sections of (c) benchmark B and (d) improved models.
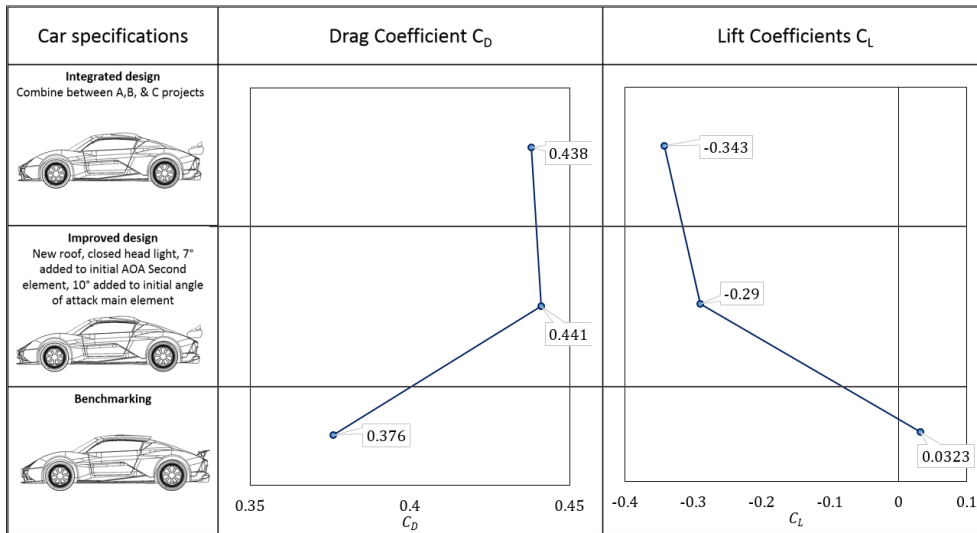
Figure B7. Drag and lift Coefficient (Benchmark and introduced designs).
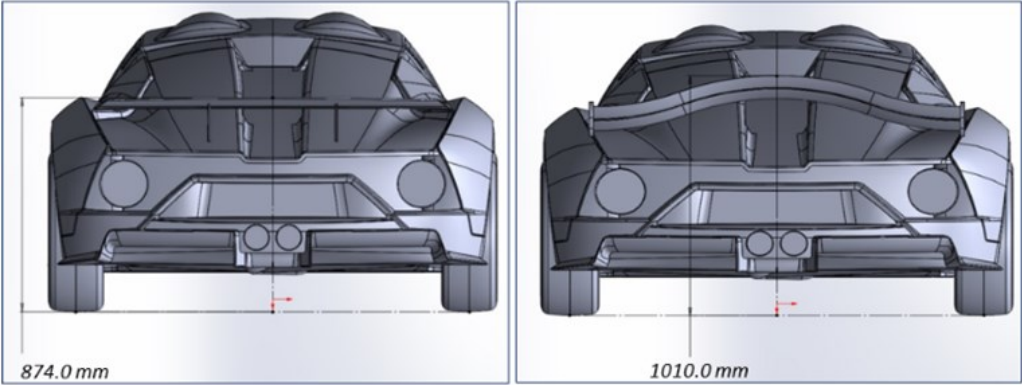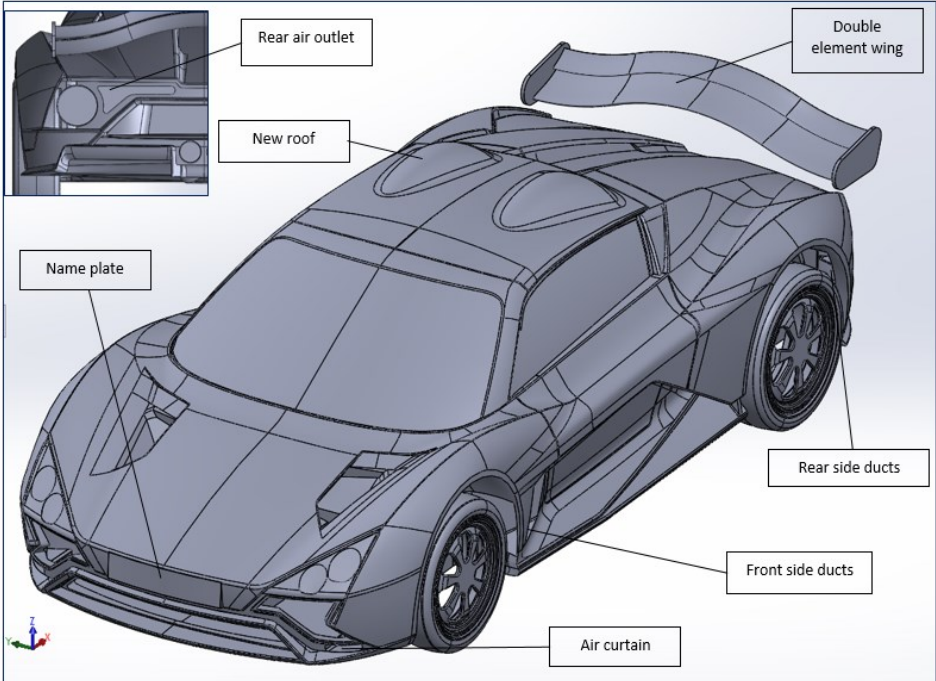
Figure B8. Shape difference between the original and new wing designs.

Figure B9. Integrated design modifications.